# PRE-SYNOPSIS SEMINAR

**ON**

# Synthesis and characterization of Inorganic semiconductor nanoparticles and their applications.

**BY**


## NeelamKumari Gupta

**Under The Guidance Of**

## Dr. Hemant P Soni

Department of Chemistry,

Faculty of Science,

The Maharaja Sayajirao University of Baroda,

Vadodara - 390002, Gujarat, India.


**12th February 2022**

# Synopsis of the Thesis

To be submitted to The Maharaja Sayajirao University of Baroda for the award of the degree of DOCTOR OF PHILOSOPHY in chemistry.

Name of Student: NeelamKumari Gupta

Title of the Thesis: "**Synthesis and characterization of Inorganic semiconductor nanoparticles and their applications".**

Name of the Supervisor: Dr. Hemant P Soni

Faculty: Faculty of Science, The Maharaja Sayajirao University of Baroda.

Department: Department of Chemistry

Registration No: FOS/2001

Date of Registration: 11th May 2016

Dr. Hemant P Soni
Research Supervisor

Prof. A V Bedekar
Offg. HEAD
Department of Chemistry

**Chapter 1: Introduction**

**Chapter 2: Benzylic $C_{sp3}$-H Bond Oxidation on (111) Facets of *o*-$Cu_2O$ Nanocrystals: C-H Bond Activation through Semiconductor Facets Mediated Catalysis.**

**Chapter 3: *c*-$Cu_2O$ Nanocrystals for Free Radical Mediated Benzylic $C_{sp3}$-H Bond Oxidation: (100) Surfaces are not always Inactive.**

**Chapter 4: Synthesis and characterization of Fe, Ni (dual Metal-Metal) doped ZnS NPs and their photocatalytic activity.**

**Chapter 5: Synthesis and characterization of Fe, B (dual Metal- Non-metal) doped ZnS NPs and their photocatalytic activity.**

## Chapter1: Introduction

Semiconductor Nps should have at least one dimension less than 100 nm. They should possess properties between metals and non-metals. They have a high Surface area; hence they are highly chemically reactive. They Have wide bandgaps, therefore showed significant alteration in their properties with bandgap tuning.

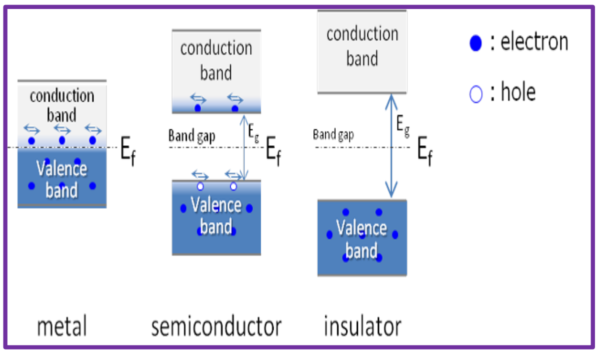


**Fig.1.1. The bandgap of Metal, Semiconductor, and Insulator**

Fig. 1.1 shows the bandgap of metal, semiconductors, and insulators. In metals, the conduction band and the valence band come very closer to each other and may even overlap, with the Fermi energy ($E_f$) somewhere inside. This means that the metal always has electrons that can move freely and so can always carry current. Such electrons are known as free electrons. These free electrons are responsible for the current that flows through a metal.

In semiconductors and insulators, the valance band and conduction band are separated by a forbidden energy gap (Eg) of sufficient width, and the Fermi energy (Ef) is between the valence and conduction band.

In semiconductors at room temperature, the bandgap is smaller, hence there is enough thermal energy to allow electrons to jump the gap fairly easily and make the transitions in the conduction band. At low temperatures, no electron possesses sufficient energy to occupy the conduction band, and thus no movement of charge is possible. At absolute zero, semiconductors are perfect insulators, the density of electrons in the conduction band at room temperature is not as high as in metals, thus cannot conduct current as good as metal. The electrical conductivity of a semiconductor is not as high as metal but also not as poor as an electrical insulator. That is why, this type of material is called semiconductor - means half conductor.

The bandgap for insulators is large so very few electrons can jump the gap. Therefore, current does not flow easily in insulators. The difference between insulators and semiconductors is the size of the bandgap energy. In an insulator where the forbidden gap is very large and as a result, the energy required by the electron to cross over to the conduction band is practically large enough. Hence insulators do not conduct electricity easily. That means the electrical conductivity of the insulator is very poor.

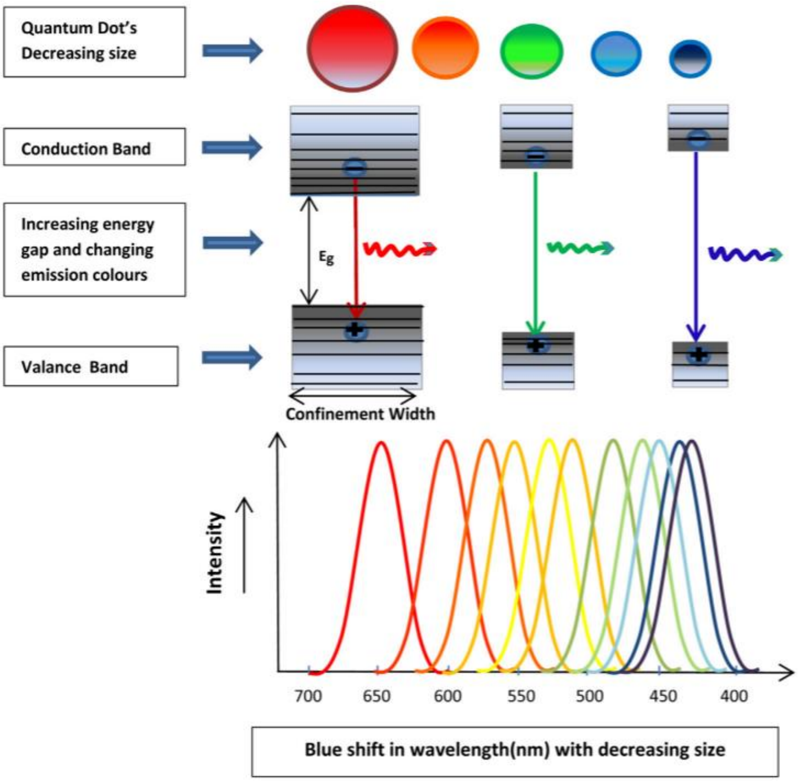


**Fig1.2 Illustration of Quantum confinement effect in the semiconductor.**

The bandgap of semiconductors can be tuned by decreasing or increasing the size of nanoparticles. On decreasing the size, the electron gets confined to the particle (confinement effects), which leads to an increase in bandgap energy and Blue-shift, Furthermore, valance band and conduction bands split into quantized energy levels. (discrete).

Recently it is found that the exposed facets of semiconductor NCs have been found to have greater versatility than size. Metal and metal oxide NCs with high index facets possess more active catalytic sites than usual due to the presence of a high density of low-coordinated atoms, edges, and corners and now it becomes an important arena in catalysis. However, those facets are unstable and hardly obtained. Thus, the shape-dependent catalysis is primarily focused on low-index facets. Facets are flat faces on particular geometric shapes. They are basically two types (i) low-index (111, 110,100) (ii) high-index (at least one index being **greater than unity**).

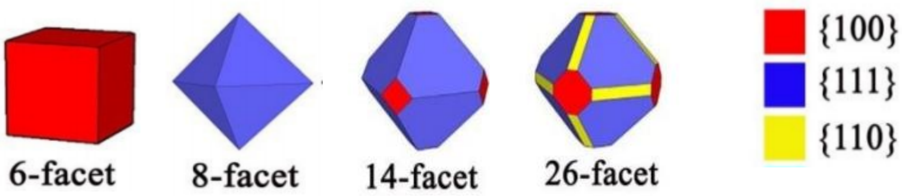


**Fig.1.3 Exposed facets.**

**During the synthesis of Nps, If the growth of the Nanoparticle is under thermodynamic control, the product will be low-index facets i.e., lower surface energy.** In this case, the capping agent plays an important role in determining the products' shape, because the different facets have different selective adsorption properties. Hence Desired shape could be achieved by altering the relative order of the surface energy of different facets using various organic or inorganic additives. Many important properties like Reactivity, photocatalytic activity, and electrical conductivity depend on exposed facets. Hence The performance of catalyst can be enhanced by shape control.

## Chapter2: Benzylic $C_{sp3}$-H Bond Oxidation on (111) Facets of Octahedral $Cu_2O$ Nanocrystals: C-H Bond Activation through Semiconductor Facets Mediated Catalysis.

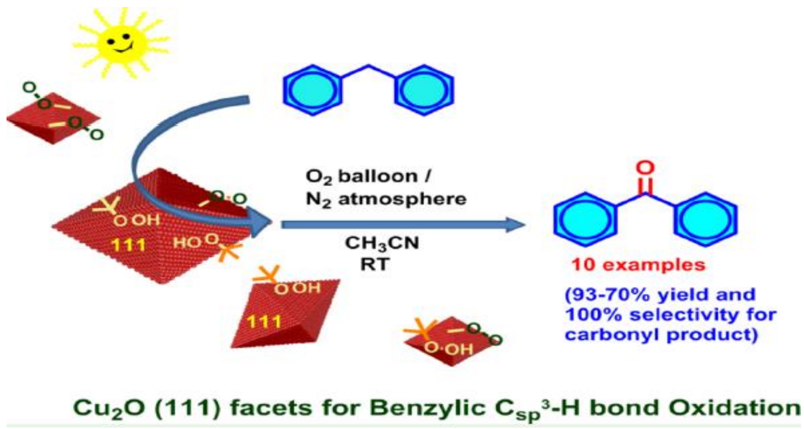


Selective functionalization of C-H bonds is challenging since it requires activation of very inactive C-H bond/s towards the reagents or catalytic systems. This protocol is important in organic synthesis as it can reduce many steps towards the target product in total synthesis and save precious resources and affect the overall cost. A wide range of commercially available pharmaceutical drugs has oxidized benzylic positions involved in their structure. For example, tiaprofenic acid, fenofibrate, tilorone Hence benzylic $C_{sp3}$-H bond oxidation is very important in the pharma industry.

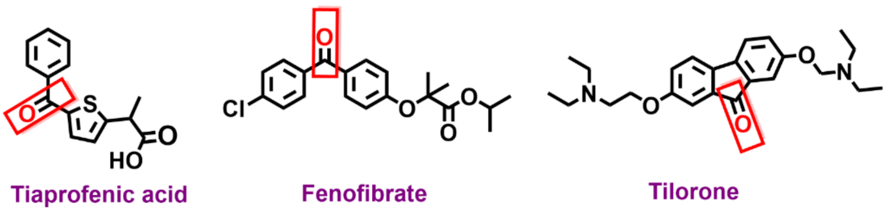

Direct oxidation of benzylic sp3 C-H to carbonyl is tricky and involves metals like Au, Pd, Rh, Ru, and Re, (of group 4d and 5d) mediating catalysis. Friedel-Crafts acylation of aromatics is a very well-known synthesis protocol for this purpose. However, it involves metal halide-based Lewis acid catalysis. Strong oxidizing agents like acidic solutions of $KMnO_4$ or $CrO_3$ can do the same job. However, these protocols pollute the environment during end processing. This, in turn, requires efficient effluent treatment plants and advanced processing technologies that can meet the stringent laws concerned with the environment.

**The objective of this work**

Development of a mild, efficient, and environmentally friendly method for benzylic C-H oxidation. None of these studies report facet-mediated catalysis for benzylic $sp^3$ C-H bond oxidation. Hence, we thought that the eight (111) facets of *o*-$Cu_2O$ NCs having Cu (I) ions with dangling bonds exposed can be the catalytic sites for benzylic $sp^3$ C-H bond oxidation.

## Synthesis of *o*-$Cu_2O$ NCs

6.0 mmol of cupric acetate ($Cu(CH_3COO)_2$. $H_2O$) and 0.12 mmol(in repeating unit) of polyvinyl alcohol (PVA) were dissolved in 50mL water at 60 $^oC$. The light blue color solution was stirred for 1h. Then, the aqueous solution of NaOH (120mmol, 4.8g in 20 mL) was added dropwise under vigorous stirring. The appearance of dark blue color indicates the formation of cupric hydroxide (Cu(OH)2). Then 20 mL aqueous solution of ascorbic acid (18 mmol) was added quickly in the above suspension under vigorous stirring and the color of the suspension changed from blue to green and finally to reddish after 30 min of stirring. The reaction mixture was centrifuged at 6000 rpm for 10 min. The collected product was washed with DI water (5 times) and finally with absolute alcohol and dried in the oven at 60 $^oC$.

**Characterization of *o*-$Cu_2O$ NCs.** The phase and purity of as-synthesized *o*-$Cu_2O$ NCs were studied by powder X-ray diffraction (PXRD). The XRD pattern manifests predominant diffraction peaks at 2θvalues of 29.65$^o$, 36.52$^o$, 42.42$^o$, 61.55$^o$, 73.73$^o$ and 77.61$^o$ corresponding to tshe X-ray diffraction pattern (Fig. 1) shows the refraction from (110), (111), (200), (220), (311) and (222) planes, respectively confirming the cuprite phase of $Cu_2O$ (JCPDS#77-0199). EDAX elemental analysis also reveals the phase purity of the material.

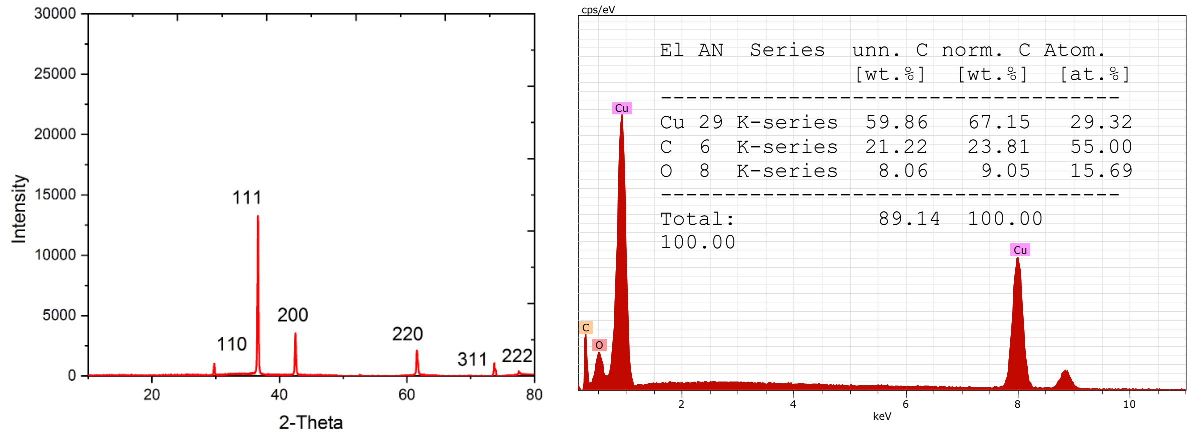


Fig.2.1 XRD patterns and EDAX elemental analysis of as-synthesized *o*-$Cu_2O$ NCs.

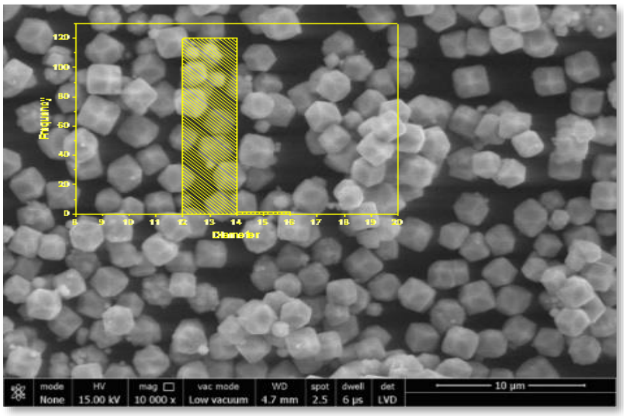


Fig.2.3 HRSEM image with size distribution histogram (inset)

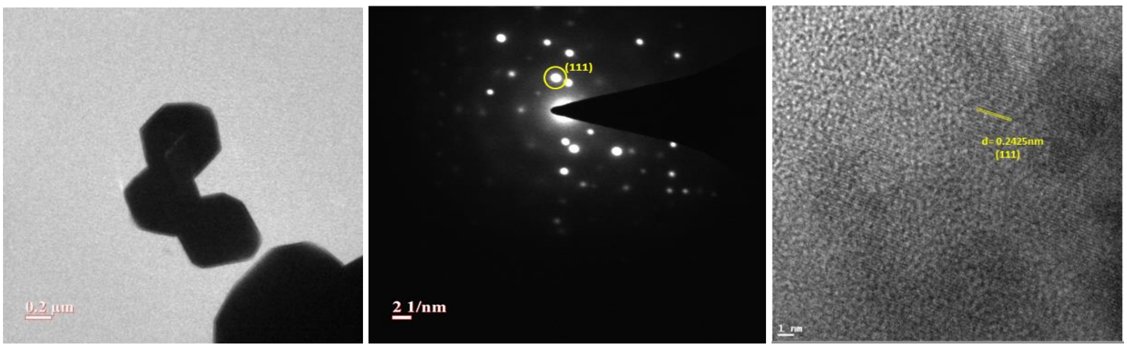


Fig.2.4 (A) HRTEM image (B) SAED pattern showing intense diffraction from {111} facets(C) lattice fringes with calculated d-spacing of *o*-$Cu_2O$ NCs

The crystallographic features of this octahedral morphology were also studied by using TEM and corresponding Selected Area Electron Diffraction (SAED) analysis. In a cluster of three hexagons, the central one is attached with the other two through (111) facets. A little truncation with the emergence of {100} planes can also be observed. A clear 125$^{o}$ angle among the sharp {111} edges can provide a site for the catalytic reaction.

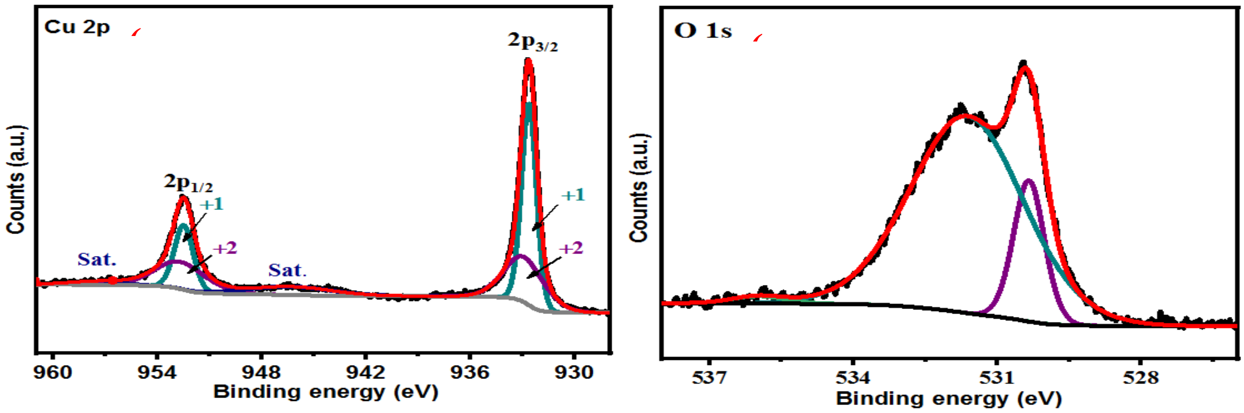


Fig.2.5 The deconvoluted XPS of (A) Cu $2p_{3/2}$ and Cu $2p_{1/2}$ of $Cu_2O$ NCs (B) O 1s spectra of $Cu_2O$ NCs.

The peak at 932.2 eV is for $Cu^{+1}$ and the peak at 952.3 eV is corresponding to the spin-orbit coupling of $Cu_2O$. A peak is at 1.8eV higher than the main peak in $O1_S$ due to the hydroxyl group.

## Experimental

As synthesized NPS were used for benzylic oxidation of small organic molecules. Our investigation began with the oxidation of DPM as a model reaction to optimize the reaction parameters.

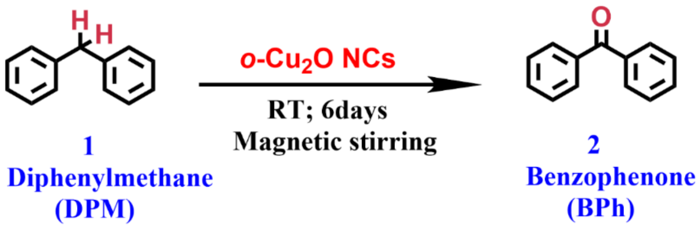


we found that around 92% yield of **2** with 100% selectivity was achieved when 1 Equiv.of **1**and 4eqiv. of TBHP were mixed in the presence of 3.5% $Cu_2O$ at RT at the end of the sixth day of the reaction under normal magnetic stirring. To get further insight into the role of catalyst, it is necessary to understand the nature of oxidation Rx$^{n}$. Literature reveals that it takes place via free radicals. So various radical scavenger experiments were performed to know which radical is involved in oxidation reaction also for the reason of color changing of catalyst.

**Table: Scavenger Experiments Carried Out to Detect the ROS Involved during the Reaction.**

| Sr. No. | Scavenger | ROSs | **Reaction I** 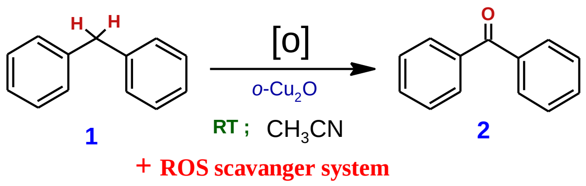  | **Reaction II** $Cu_2O \xrightarrow{[o]} CuO$ dark Red / Blue |
|---|---|---|---|---|
| 1 | Isopropyl alcohol (0.01 M) | $\cdot OH$ | Complete conversion with 100% selectivity on the fourth day of the reaction. | Starts on third day with residual $Cu_2O$ on the wall of the reactor. |
| 2 | KI (0.01 M) | Surface adsorbed $\cdot$OH or $^+h$ | Complete conversion with 100% selectivity on the fourth day of the reaction. | Starts on third day with residual $Cu_2O$ on the wall of the reactor. |
| 3 | $KBrO_3$ (0.01 M) | $e^-$ | 90% yield | No reaction |
| 4 | $KBrO_3$ (0.01 M) + KI (0.01 M) | $e^- + {}^+h$ | 90% yield | No reaction |
| 5 | Ascorbic acid (30 mM) | $O_2^{\cdot -}$ | 20% yield | No reaction |
| 6 | Benzoquinone (30 mM) | $O_2^{\cdot -}/HO_2^{\cdot}$ | 25% yield | No reaction |
| 7 | Isopropyl alcohol (30 mM) + benzoquinone (30 mM) | $HO^{\cdot}$ + $O_2^{\cdot -}/HO_2^{\cdot}$ | 30% yield | No reaction |

From all the above experiments it can be concluded that $OH^{\cdot}$ is not responsible for both reactions, Surface adsorbed $O_2^{\cdot -}$ is the primary requirement of catalyst vaporization but only in presence of light. By combining all experiments we proposed a mechanism under nitrogen and under aerial conditions.

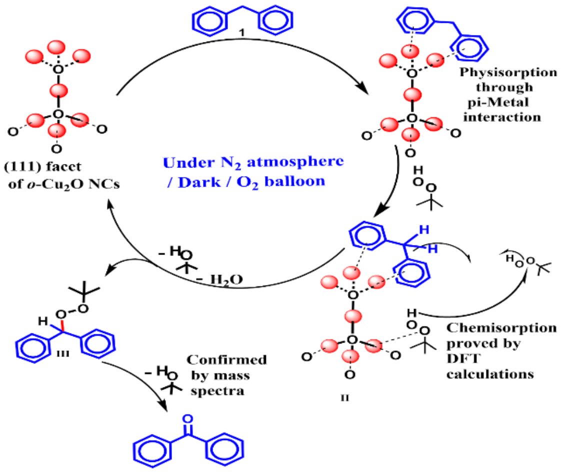


Scheme 2.1. Proposed reaction mechanism of benzylic sp$^3$ C-H oxidation of 1 with TBHP in presence of *o*-$Cu_2O$ NCs in $N_2$ atmosphere and light. red balls indicate $Cu^{1+}$ ions.

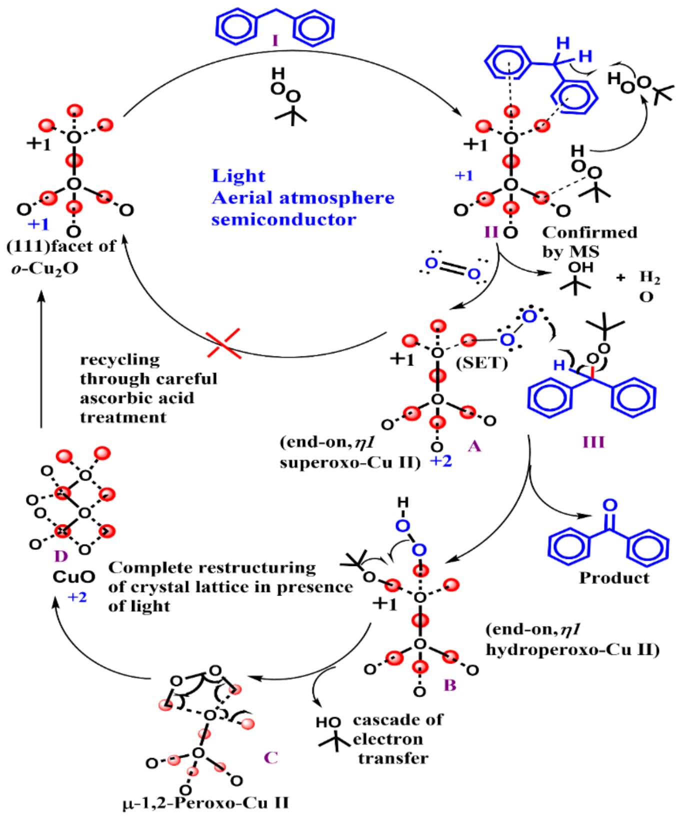


Scheme 2.2 Proposed reaction mechanism of benzylic sp$^3$ C-H oxidation of 1 with TBHP in presence of *o*-$Cu_2O$ NCs in aerial atmosphere and light. red balls indicate $Cu^{1+}$ ions.

## Conclusion

(111) faceted $Cu_2O$ nanocrystals having octahedral morphology have been synthesized and characterized. The exposed (111) facets of $Cu_2O$ NCs were explored as catalytic sites for the

benzylic $sp^3$C-H bond oxidation process. From the optimization of model reaction, free radical scavenger experiments, and special experiments, the following conclusions can be drawn: (1) $Cu^{1+}$ ended (111) facets of o-$Cu_2O$ NCs are capable to activate dioxygen molecules to undergo reduction by a SET mechanism in presence of light, and the in situ generated superoxide species immediately abstract the ·H radical from the nearby substrate initiates the cascade of chemical reactions and electronic processes resulting into stable oxidation product and a complete restructuring of the crystal lattice of the catalyst, respectively. (2) The etching of the (111) surface during the oxidation process can be avoided if the reaction is carried out in dark or under an inert atmosphere or under a continuous flow of dioxygen gas. (3) The developed protocol for benzylic $sp^3$C-H bond oxidation to a ketone is applicable under mild conditions with 100% selectivity just by stirring the reaction mixture for 4 days (4) Also, this protocol is equally and effectively applied to the wide range of substrates having C-H bond energy less than 90 kcal/mol. (5) The (111) facets of o-$Cu_2O$ NCs can be regenerated for the next three catalytic cycles with minute loss in reactivity by maintaining the proper reaction conditions.

# Chapter 3: *c*-$Cu_2O$ Nanocrystals for Free Radical Mediated Benzylic $C_{sp3}$-H Bond Oxidation: (100) Surfaces are not always Inactive.

In the present study, we have synthesized cubic (100) (c-$Cu_2O$, Cc), rhombic dodecahedral (110) (d-$Cu_2O$, Dh), and octahedral (111) (o-$Cu_2O$, Oh) faceted $Cu_2O$ NCs and compared their activities for benzylic $sp^3$ C-H bond oxidation of DPM under the optimized reaction parameters with t-butyl hydroperoxide (TBHP) as an oxidant and aerial atmosphere.

## Preparation of catalyst.

| | Volume of DI | $CuCl_2$(0.1M) | SDS Sodium dodecyl sulfate | NaOH(1.0M) | $NH_2OH.HCl$ (0.1M) |
|---|---|---|---|---|---|
| ***d*-$Cu_2O$ (110)** | 223ml | 25ml | 4.35g | 9ml | 120ml |
| ***c*-$Cu_2O$ (100)** | 173ml | 25ml | 4.35g | 9ml | 20ml |

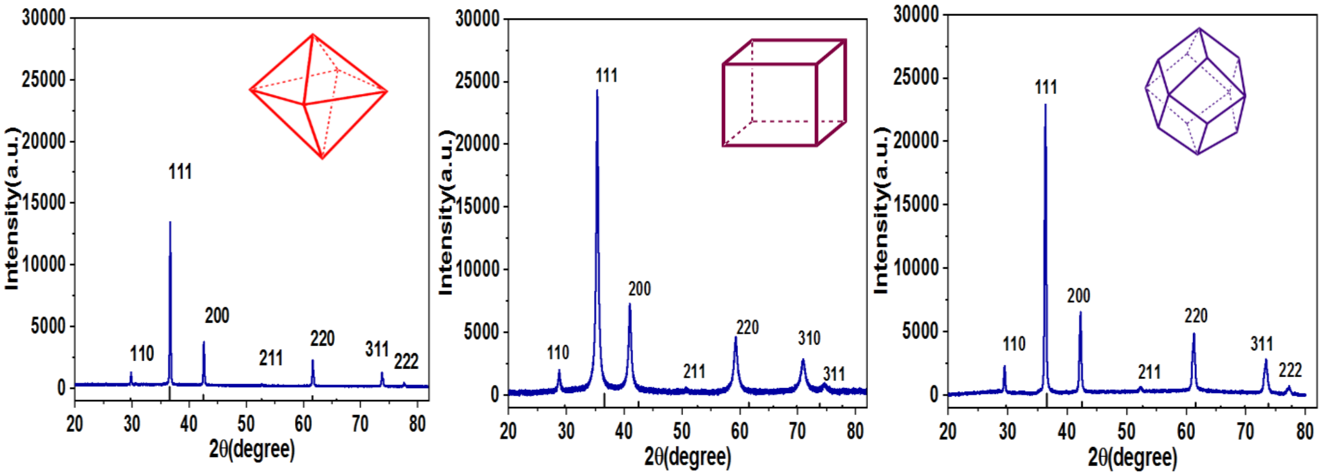


Fig.3.1 XRD patterns of as-synthesized (a) octahedral(Oh) (b) cubic (Cc) (c) dodecahedral (Dd) $Cu_2O$ NCs (JCPDS#77-0199).

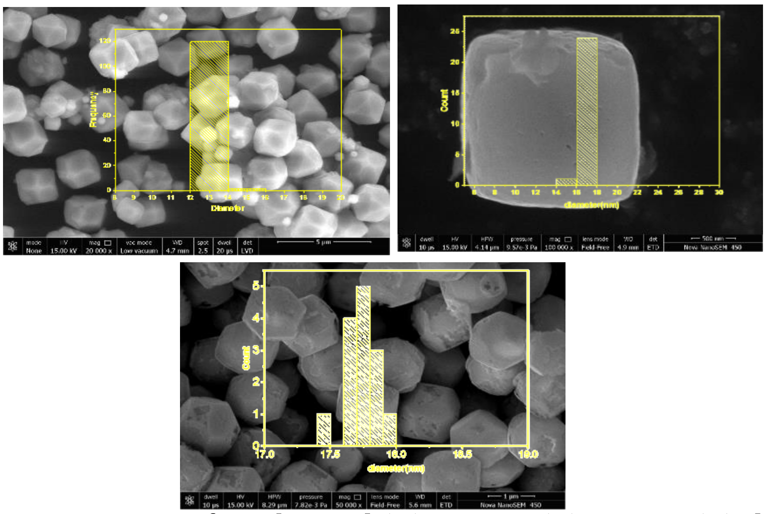

Fig.3.2 FESEM images of synthesized (A) *o*-$Cu_2O$ (B) *c*-$Cu_2O$ (C) *d*-$Cu_2O$ NCs.

The phase and purity of as-synthesized $Cu_2O$ NCs of three different morphologies were studied by powder X-ray diffraction (Fig. 1). The diffraction peaks at 2θ values, 29.65°, 36.52°, 42.42°, 61.55°, 73.73° and 77.61° are indexed to (110), (111), (200), (220), (311) and (222) planes, respectively, confirming the cuprite phase of $Cu_2O$ (JCPDS#77-0199) with a lattice constant of 4.26 Å having body-centered cubic packing of oxygen atoms and copper atoms occupying half of the tetrahedral sites. It can be observed from the XRD pattern that the (111)/(200) ratio for the Oh morphology is the highest due to predominantly exposed {111} facets and it is the least in the case of cubic morphology. The morphologies of as-synthesized $Cu_2O$ NCs were also studied by FESEM analysis (Fig. 3.2). FESEM images display clear and uniform size distribution.

## Experimental

We had optimized the parameters for this protocol also as our previous study that was carried out in presence of *o*-$Cu_2O$ NCs.

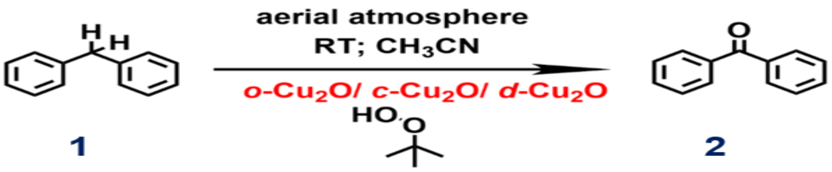


Table 3.1 Oxidation of the benzylic sp$^3$ C-H bond in presence of $Cu_2O$ NCs having various morphologies.

| **Sr. No.** | **Morphology** | **Major surfaces exposed for catalysis** | **Reaction time (time required to complete the reaction) (days)** | **Yield [a] (at the end of reaction) (%)** | **Observations** |
|---|---|---|---|---|---|
| 1 | c-$Cu_2O$ | {100} | 3 (3) | 98 (99) | No leaching/valorization of the catalyst |
| 2 | o-$Cu_2O$ | {111} | 3 (5) | 80 (92) | Complete catalyst valorization |
| 3 | d-$Cu_2O$ | {110} | 3 (4) | 88 (92) | Partial catalyst valorization in the stipulated time period |

It can be observed from Table 1 that the model reaction takes the highest completion time (5 days) in presence of *o*-$Cu_2O$ with 92% yield. While the same reaction yield was obtained within 4 days in the presence of *d*-$Cu_2O$. It is interesting to note that the reaction takes minimum completion time in presence of *c*-$Cu_2O$ NCs with 98% yield at the end of 3$^{rd}$ day.

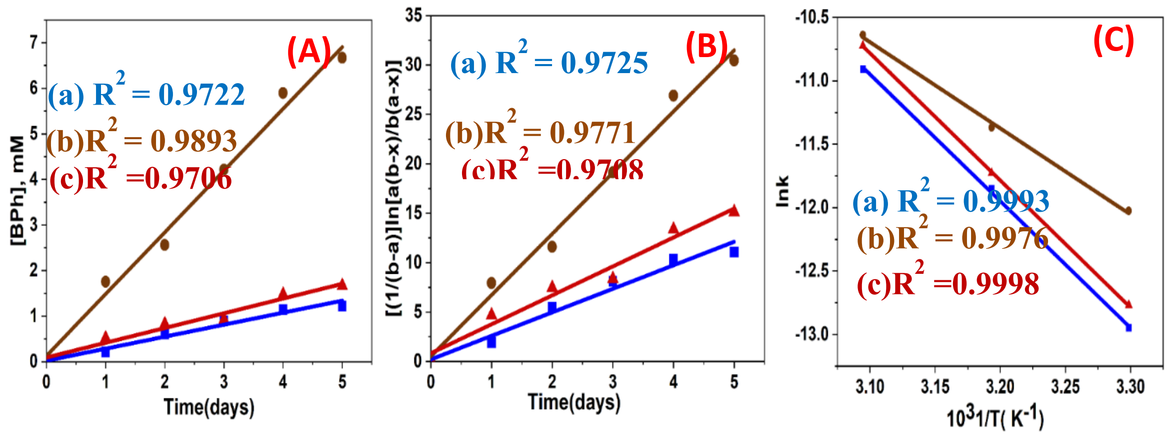


Fig.3.3 For 1 mmol DPM (A) Product [BPh] vs time and (B) Rate constant ($mol_{DPM}L^{-1}$ $day^{-1}$) of $Cu_2O$ (a) octahedral (b) cubic and (c) dodecahedral as a function of time (C) Arrhenius plot for $Cu_2O$ octahedral (a), cubic (b), and dodecahedral (c) shapes.

To find out the path through which reaction has proceeded, a chemical kinetics study is very important. . Hence, from these data, [product] Vs. time was plotted (Fig.6A) (TableS5) and the slope of these graphs gives initial rates (TableS7). Rate constants were obtained from the slope of the graph $\frac{1}{b-a} ln \frac{a(b-x)}{b(a-x)}$ Vs. time (b > a) (Fig. 6B) (Table S6). It can be observed that cubic morphology shows the highest value of the rate constant for all the concentration range. Apparent activation energy, calculated for all the facets catalysed reactions at 303, 313, and 323K by using the Arrhenius equation and slope of the Arrhenius plots), is 80.09, 56.48, and 83.34 kJ/mol for *o*- $Cu_2O$, *c*- $Cu_2O$, and *d*- $Cu_2O$, respectively (Fig. 6C).[35] It is confirmed from the kinetics studies that the overall order of the oxidation process is second-order (Fig. 6B) and it is the first order to [DPM]. Hence, DPM and TBHP both are required to proceed the reaction. The calculated apparent activation energy for *c*-$Cu_2O$ NCs is much smaller than the NCs of other morphologies. These results suggest higher intrinsic activities at the oxygen-ended *c*-$Cu_2O$ surfaces.

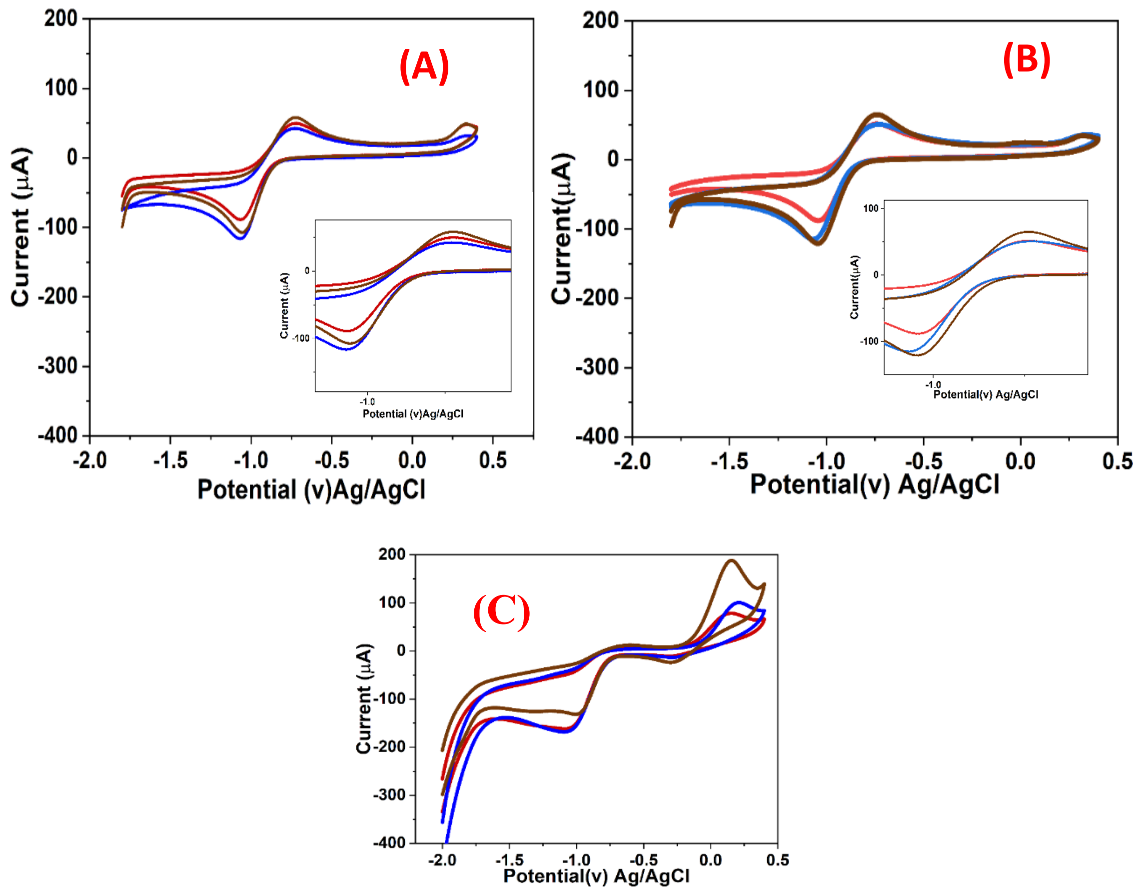

Fig.3.4 Cyclic voltammograms of (A) Blank (only with catalyst, [(a) *o*-$Cu_2O$ (b) *c*-$Cu_2O$ (c) *d*-$Cu_2O$]); inset shows enlarged image for the same (B) after addition of DPM (catalyst + DPM [(a) *o*-$Cu_2O$ (b) *c*-$Cu_2O$ (c) *d*-$Cu_2O$] scan rate of 50 $mVs^{-1}$) (C) after addition of TBHP (catalyst + DPM + TBHP [(a) *o*-$Cu_2O$ (b) *c*-$Cu_2O$ (c) *d*-$Cu_2O$]).

To have a deeper idea about the electronic processes taking place on the various surfaces during a chemical reaction, electrochemical analyses were carried out. The reversible CV response is obtained for NCs of all the morphologies at a given scan rate proving the suitability of the material for catalytic activities under the given reaction conditions (Fig. 3.4A). Now, on introducing DPM in the system having $Cu_2O$ NCs coated glassy carbon electrode dipped in acetonitrile, the current density for both the scan rates equally increases (Fig. 3.4B). It is highest in the case of c-$Cu_2O$ NCs confirms the adsorption and electronic interaction of DPM with the surface and absence of any additional redox couples or peaks denying the possibility of any other electrochemical processes under prevailing conditions.

**Mechanism**

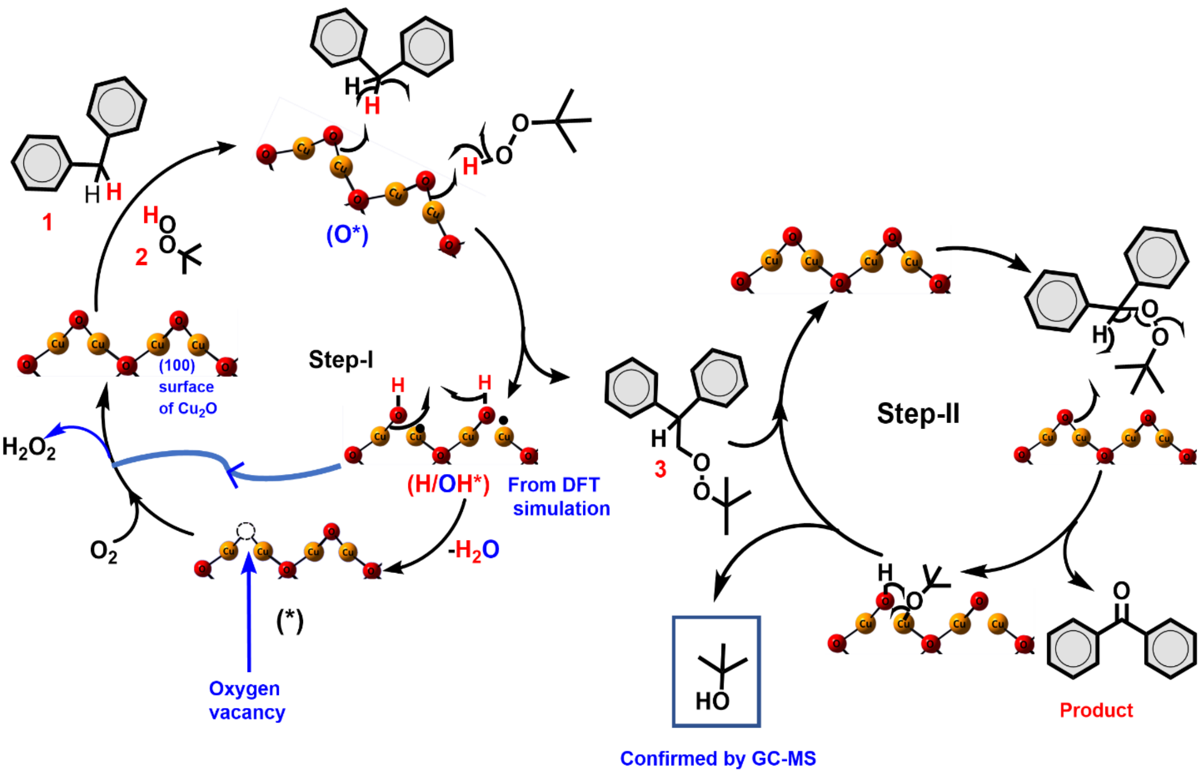


Scheme 3.1 Proposed reaction mechanism of benzylic $sp^3$ C−H bond oxidation of DPM with TBHP in the presence of *c*-$Cu_2O$ NCs in the aerial atmosphere.

It can be observed from Scheme 3.1 that DPM (1) gets adsorbed through H-bonding with oxygen of $Cu_2O$ (100) surface, in turn, TBHP is also chemisorbed in the vicinity on the surface, resulting in the cascade of the chemical events. Firstly, (100) surface lattice O-atoms ($O^*$)

abstract H-atoms from the DPM and TBHP resulting in peroxo intermediate 3 which takes part in the second catalytic cycle leading to the product. These initial events generate two-electron reduced centers consisting of vicinal hydroxyl groups (H/OH*), which in turn, generate oxygen vacancies (*) on the surface by ejecting the water molecule. Now, the reoxidation process of this oxygen vacancy is fast and an issue of debate. The reoxidation by $O_2$ molecule involves the following events: (1) activation of $O_2$ molecule by (*) resulting superoxide species (2) breaking of O-O bond resulting (100) surface lattice (O*) and one O atom (3) hopping of the O atom via lattice diffusion to refill another reduced center or oxidize the other species in the vicinity. The detailed study is out of the scope of this work. But, we can propose that the O atom may oxidize the water molecule into $H_2O_2$ again decompose into two water molecules in the catalytic loop and complete the cycle (Scheme 3.1). We recycled the c-$Cu_2O$ for three consecutive cycles without affecting the % yield of the reaction.

## Conclusion

(100), (111), and (110) faceted $Cu_2O$ NCs having Cc, Oh, and Dh morphologies, respectively have been synthesized and characterized. oxygen ended (100) facets of cubic $Cu_2O$ NCs can do the oxidation process faster than any other facet. It can be claimed that oxygen-ended c-$Cu_2O$ (100) surfaces are inactive for photo-physical and photochemical processes like dye degradation. But these {100} surface planes are highly active for metal oxide semiconductor-based oxidation processes. The surface ends oxygen atoms first abstract the ˙H from the DPM and TBHP, forming the hydroperoxide take part in the second catalytic cycle for the product generation, leaving the oxygen vacancies/reduced center on the metal oxide surface. The resulting reduced center activates the aerial oxygen molecule to refill the vacancies and regenerate the catalytic surface.

# Chapter 4: Synthesis and characterization of Fe, Ni (dual Metal-Metal) doped ZnS NPs and their photocatalytic activity.

## literature

Heterogeneous photocatalysis using metal sulfide semiconductor Nps is widely recognized as an effective technology for wastewater treatment. From the literature, it is found that ZnS is having remarkable properties among all the metal sulfides. ZnS is one of the most widely investigated photo-catalysts because it rapidly generates electron-hole pairs under photoexcitation, and exhibits a relatively high photocatalytic activity under UV light. Photo-catalytic activity can be enhanced by doping or introducing impurities. Purpose of the study is to synthesize the mono-doped and dual-doped ZnS NPS for complete dye degradation. In this study, we have prepared Fe and Ni dual doped ZnS at 7% of each i.e. ($Fe_{0.07}Ni_{0.07}$) and at 5% of each dopant i.e. ($Fe_{0.05}Ni_{0.05}$) while mono doped samples of each dopant have also been prepared for comparative study.

## Synthesis.

Zinc acetate dihydrate $(CH_3COO)_2Zn.2H_2O$) AR grade sigma Aldrich, Ferrous tetrachloride tetrahydrate ($FeCl_2.4H_2O$) AR grade Merck, Nickel acetate tetrahydrate ($(CH_3COO)_2Ni.4H_2O$) AR grade Merck were used as dopants. Sodium hydroxide (NaOH) AR grade Merck, Sodium sulfide ($Na_2S.xH_2O$) AR grade Loba Chemie, 2-Mercaptoehanol ($HSCH_2CH_2OH$) AR grade sigma Aldrich, RhodamineB ($C_{28}H_{31}ClN_2O_3$) S.D. fine chemicals.All reagents were used without any further purification. 2-Mercaptoethanol was used as a capping agent. In a typical procedure, $5\times10^{-3}$ mol of Zinc acetate was dissolved in 200 ml D.I water. 50 ml of each dopant ($11.49\times10^{-5}$mol, for $Fe_{0.07}$ and $9.18\times10^{-5}$mol, for $Ni_{0.07}$) and ferrous chloride ($8.19\times10^{-5}$mol, $Fe_{0.05}$ and $6.56\times10^{-5}$, for $Ni_{0.05}$) were added dropwise under vigorous stirring. Stirring was continued for 40 min until complete dissolution of both dopants. During the experiment, the pH of the solution was maintained at 11 using an aqueous solution of NaOH (1M), followed by dropwise addition of 2-mercaptoethanol (0.025mol in 50ml). The temperature of the reaction mixture was gradually raised to 70°C. The reaction mixture was stirred thoroughly for a further half an hour to obtain a homogenous mixture. To this $Na_2S$ solution, ($5\times10^{-3}$mol in 50 ml) was added dropwise at the rate of 1mL /min. The reaction mixture was further stirred for 3hr to obtain homogenous stabilized dispersion and then allowed to cool naturally. The mixture was centrifuged at 6000 rpm for 5 min and washed with DI water 4 times and finally with absolute alcohol to remove impurities. The resulting precipitate was dried at 60°C. The color of ZnS: Fe: Ni co-doped samples was brown. Pristine ZnS was also synthesized by the same method without using dopants.

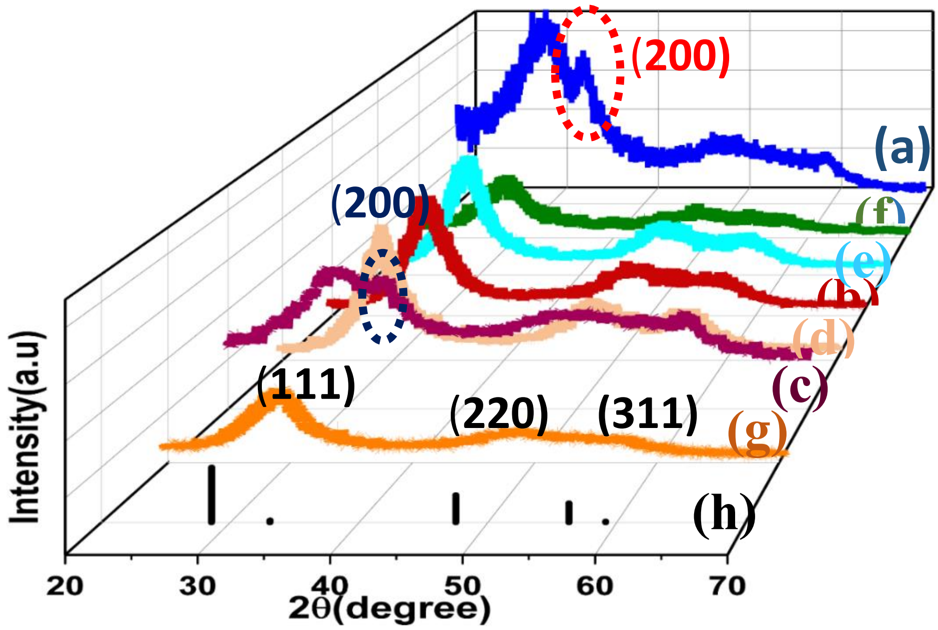


Fig. 4.1 PXRD of ZnS (a) $Fe_{0.07}Ni_{0.07}$ (b) $Fe_{0.05}Ni_{0.05}$ (c)$Fe_{0.07}$ (d) $Fe_{0.05}$ (e) $Ni_{0.07}$ (f) $Ni_{0.05}$ (g) Pristine (h) Bulk. (JCPDS 00-001-0792).

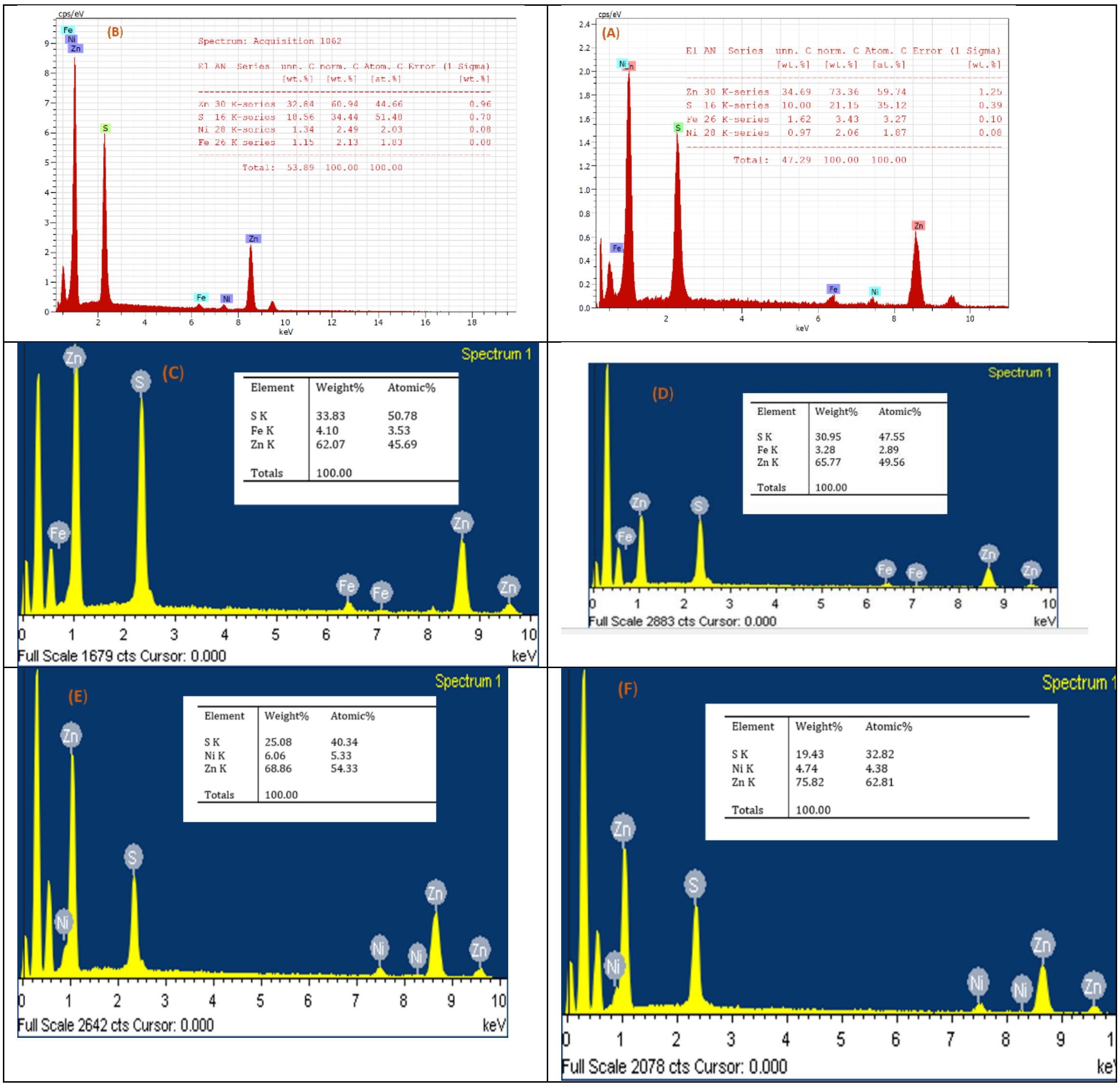


Fig.4.1 EDX spectra of synthesized ZnS NPs (a) ZnS: $Fe_{0.07}$ $Ni_{0.07}$ (b) ZnS: $Fe_{0.05}$ $Ni_{0.05}$ (c) ZnS: $Fe_{0.07}$ (d) ZnS: $Fe_{0.05}$ (e) ZnS: $Ni_{0.07}$ (f) ZnS: $Ni_{0.05}$ (G) Pristine.

PXRD analysis shows the amorphous nature of all synthesized samples. EDX spectra reveals that dopants are successfully incorporated.

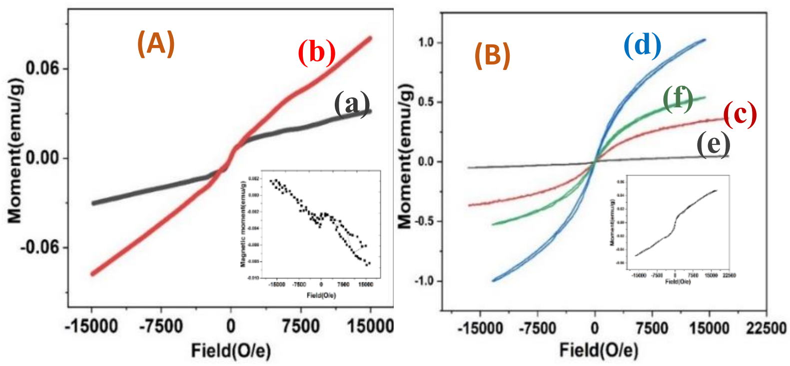

Fig. 4.3 (A)VSM (a)$Fe_{0.07}Ni_{0.07}$ (b)$Fe_{0.05}Ni_{0.05}$ (inset pristine ZnS) (B) (c) $Fe_{0.07}$ (d) $Fe_{0.05}$ (e)$Ni_{0.07}$ (f) $Ni_{0.05}$ (inset; enlarge of $Ni_{0.07}$).

Room temperature vibrating sample magnetometer analysis was carried out to know the magnetic behavior of all synthesized samples.

## Experimental

The photocatalytic performance of ZnS NPs was evaluated using RhB solution in terms of change in intensity of $\lambda_{max}$ 545 nm. Time-dependent UV–vis absorption spectra of RhB solution during photo-irradiation in the presence of synthesized NPs were recorded. The quenching of the color intensity of the solution indicates the degradation of dye with time.

**Degradation of an aqueous solution of RhB dye under white light irradiation after 320 min.**

| % Fe, Ni | % Degradation | Rate constant ($h^{-1}$) | correlation coefficient (R) |
|---|---|---|---|
| Pristine Zns | 47.69 | 0.1906 | 0.972 |
| $Fe_{0.07}$ $Ni_{0.07}$ | 79.06 | 0.2934 | 0.943 |
| $Fe_{0.05}$ $Ni_{0.05}$ | 97.12 | 0.6655 | 0.9349 |
| $Fe_{0.07}$ | 74.60 | 0.2571 | 0.9532 |
| $Fe_{0.05}$ | 72.23 | 0.1818 | 0.943 |
| $Ni_{0.07}$ | 65.87 | 0.2017 | 0.9678 |
| $Ni_{0.05}$ | 69.13 | 0.2220 | 0.984 |
| Without any catalyst | 14.13 | 0.0285 | 0.956 |

## Conclusion

Pristine, mono-doped, and dual-doped ZnS NPs at different amounts of Fe and Ni (5.0%, 7.0% by wt) were synthesized and characterized. the XRD patterns suggest that at 7.0 % dopant concentration the phase of ZnS changes from cubic to hexagonal wurtzite. Inducing co-dopants in a material, synergistically enhance the efficiency of the catalyst. 5.0% Fe, Ni co-doped ZnS NPs show optimum photocatalytic activity due to Maximum surface stabilization. And S atom acts as an efficient bridge forming charge transfer channel between TM, activates the whole surface. Hence the high photocatalytic activity of co-doped ZnS.

# Chapter 5: Synthesis and characterization of Fe, B (dual Metal-Non-Metal) doped ZnS NPs and their photocatalytic activity (under progress).

### Characterization

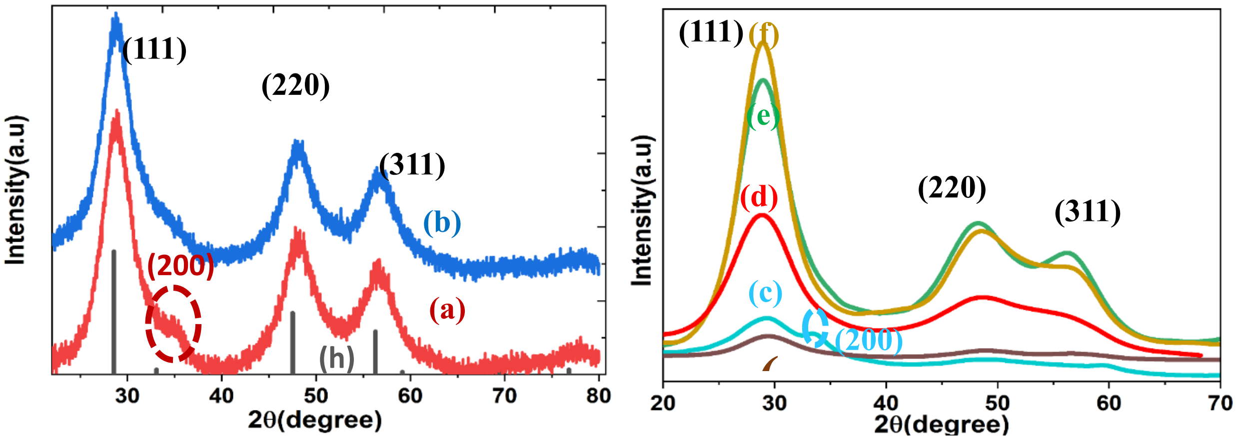


Fig.5.1 PXRD of synthesized co-doped NPs with (a) $Fe_{0.07}B_{0.07}$ (b) Fe $_{0.05}B_{0.05}$ (c) $Fe_{0.07}$ (d) $Fe_{0.05}$ (e) $B_{0.07}$ (f) $B_{0.05}$ (g) Pristine ZnS (h) Bulk ZnS.

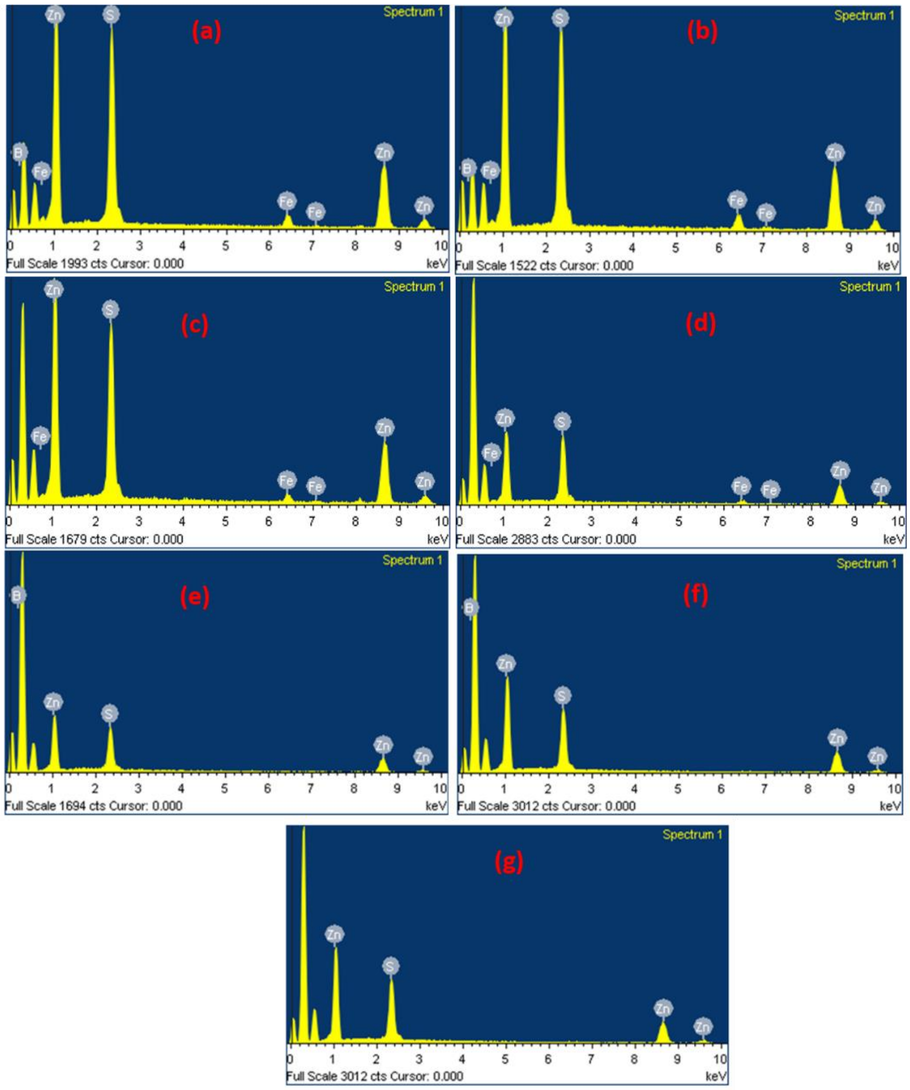


Fig. 5.2. EDX spectra of synthesized (a) Fe $_{0.07}B_{0.07}$ (b) $Fe_{0.05}B_{0.05}$ (c) $Fe_{0.07}$ (d) $Fe_{0.05}$ (e) $B_{0.07}$ (f) $B_{0.05}$ (g) Pristine ZnS nanoparticles.

PXRD analysis shows the amorphous nature of all synthesized samples. EDX spectra reveal that dopants are successfully incorporated.

## Conclusion

Pristine, monodoped, and co-doped ZnS NPs at different amounts of Fe and B (5.0%, 7.0% by wt) were synthesized and characterized. The XRD patterns suggest that at 7.0 % dopant concentration in both mono and co-doping, the phase of ZnS changes from cubic to hexagonal wurtzite. Inducing co-dopants in a material, synergistically enhance the efficiency of the catalyst to make the aqueous solution colorless. At 5.0% Fe, B co-doped ZnS NPs show optimum photocatalytic activity due to Maximum surface stabilization due to charge distribution. As the amount of co- dopant ions increases from 5.0 to 7.0%, photocatalytic efficiency decreases.

## References


D. Berney Needleman, "Optical design guidelines for spectral splitting photovoltaic systems: A sensitivity analysis approach," M.S. thesis, Dept. Mech. Eng., Mass. Inst. Technol., Cambridge, MA, USA, 2014

Takagahara, T.; Takeda, K. Theory of the quantum confinement effect on excitons in quantum dots of indirect-gap materials. *Phys. Rev. B* **1992,** 46 , 15578.

- B, Ni.; Wang, X. Catalytic Active Sites of Nanomaterials. *Adv Sci.* **2015**, 2, 1500085.
- Xiao, Chi.; Lu, Bang-An.; Xue, Peng .; Tian, Na.; Zhou, Zhi-You .; Xiao, Lin.; Lin, Wen-Feng.; Sun, Shi-Gang. *Joule*. **2020**, 4, 2562-2598.

Zhang, Wei-Bing.; Chen, Chuan.; Zhang, Shun-Ying. Equilibrium Crystal Shape of Ni from First Principles. *The Journal of Physical Chemistry C*. **2013**, 117, 21274–21280

- Torres-Martínez, C.L.; Kho, R.; Mian, O.I.; Mehra, R.K. Efficient photocatalytic degradation of environmental pollutants with mass-produced ZnS nano-crystals. *J. Colloid Interface Sci*. **2001** 240, 525–532.
- Beydoun, D.; Amal, R.; Low, G.; McEvoy, S. *J. Nanoparticle Res*. **1999,** 439–458.
- Ferreira, K.N.; Iverson, T.M.; Maghlaoui, K.; Barber, J.; Iwata, S. Architecture of the photosynthetic oxygen-evolving. *Center. Science.* **2004**, 303, 1831– 1838.
- Fukuzumi, S.; Ohkubo, K. ; Suenobu, T. Long-lived charge separation and applications in artificial photosynthesis. *Acc. Chem. Res.* **2014**, 47 1455– 1464.
- Pouretedal, H.R.; Norozi, A.; Keshavarz, M.H.; Semnani, A. Nanoparticles of zinc sulfide doped with manganese, nickel and copper as nanophotocatalyst in the degradation of organic dyes. *J. Hazard. Mater.* **2009**, 162, 674–681.
- Aarthi, T.; Narahari, P.; Madras, G. Photocatalytic degradation of Azure and Sudan dyes using nano $TiO_2$. *J. Hazard. Mater.* **2007,** 149, 725–734.
- Fu, H.; Pan, C.; Yao, W.; Zhu, Y. Visible-light-induced degradation of rhodamine B by nanosized $Bi_2WO_6$. *J. Phys. Chem. B* **2005,** 109, 22432–22439.

- Mahmood, Q.; Hassan, M.; Noor, N.A. Theoretical Study of Electronic, Magnetic, and Optical Response of Fe-doped ZnS: First-Principle Approach. *Journal of Superconductivity and Novel Magnetism*, **2017**, *30*, 1463-1471.
- Momin, M.A.; Islam, M.A.; Majumdar, A.; Influence on structural, electronic and optical properties of Fe doped ZnS quantum dot: A density functional theory-based study. *International Journal of Quantum Chemistry*, **2021**, 121, 26786.



| | |
|---|---|
| NeelamKumari Gupta | Dr. Hemant P Soni |
| Research Scholar | Research Supervisor |
| | Dept. of Chemistry |